

# A High Precision Pulse Generation and Stabilization System for Bolometric Experiments

P. Carniti<sup>a,b</sup>, L. Cassina<sup>a,b\*</sup>, A. Giachero<sup>a,b</sup>, C. Gotti<sup>a,b</sup>, G. Pessina<sup>a,b</sup>

December 14, 2024

a) INFN, Sezione di Milano Bicocca, Piazza della Scienza 3, 20126, Milano, Italy

b) Dipartimento di Fisica G. Occhialini, Università degli Studi di Milano Bicocca,  
Piazza della Scienza 3, 20126, Milano, Italy

## Abstract

Bolometric experiments searching for rare events usually require an extremely low radioactive background in order to prevent that spurious signals may mimic those of interest and spoil the sensitivity of the apparatus. In such contexts, radioactive sources cannot be used to produce a known signal to calibrate the measured energy spectrum during the data taking. In this paper we present an alternative approach to stabilize the response of bolometers, based on an electronic device designed to provide an ultra-stable and very precise calibrating pulse. The instrument is characterized by the presence of multi-outputs, a completely programmable pulse width and amplitude, a dedicated daisy-chained optical trigger line and can be fully controlled and monitored from remote via CAN bus protocol. An energy resolution of the order of 10 ppm FWHM at 1 MeV and a thermal stability of the order of 0.1 ppm/°C has been achieved. The device can also provide an adjustable power to compensate for the low frequency thermal fluctuations that typically occur in cryogenic experiments.

## 1 Introduction

The researches for rare events is of great importance in modern particle physics, as they make possible to thoroughly test the Standard Model predictions. In particular, a powerful tool to study neutrino physics and dark matter consists of looking for very rare spontaneous nuclear decays or nuclear scatterings due to its interaction with a Weak Interacting Massive Particle (WIMP). Such class of experiments, which usually need long lifetime (several years) in order to collect an adequate statistics, typically requires an extremely low radioactive background and an excellent energy resolution. Among the various experimental approaches, bolometric detectors are very promising as they ensure very good intrinsic energy resolution, no dead areas, a wide choice of material and the potential to compose very large detectors. Bolometers are calorimeters operating at cryogenic temperature in which the energy released by an interacting particle

---

\*lorenzo.cassina@mib.infn.it

is measured from the consequent temperature increase. One of the most important feature that must be ensured by the electronic equipments is the response stability over the whole lifetime. As the gain of the detector strongly depends on its operating temperature, its response must be stabilized against the low frequency thermal instabilities which unavoidably affects the cryogenic system.

One way to do this is based on using a  $\gamma$ -ray source, that emits monochromatic particles absorbed by the bolometers. These signals result in a narrow peak in the energy spectrum centered at a fixed energy, only dependent on the decay mode. The peak location is known a priori so that it can be used as an absolute reference for the energy spectrum calibration. Nevertheless, a radioactive source permanently left close to the sensitive apparatus is incompatible with the experiment requirements as it would increase the radioactive background and reduce the overall sensitivity.

An alternative approach consists on mimic a particle interaction by delivering a voltage pulse across a resistive heater glued on the bolometer crystal, so that thermal power can be produced by Joule effect. The calibrating signal is a square pulse having a width ( $T$ ) much shorter than the detector response ( $\tau_B$ ), which usually has a very slow time constant ( $\tau_B \sim 1$  s) given by the product between the crystal thermal capacitance (few nJ/°K) and the thermal conductivity towards the cooling reference. Beside keeping low the radioactive budget, another merit of this solution is the complete control of the pulse generation procedure, as the pulse amplitude and width can be tuned to stabilize each detector over the full dynamic range. The pulse delivery can be also triggered from the slow control, allowing to easily tag the calibrating pulses and to generate them with a selectable rate. While the power consumed on the heating resistor is controlled from the pulse parameters, the energy injected into the bolometers is proportional to the thermal coupling between the heating resistor and the crystal ( $\eta$ ). This constant is not known a priori and changes from crystal to crystal. Unlike using a radioactive source, the pulses generated by Joule effect do not represent an absolute reference although extremely accurate and stable signals can be produced.

The solution proposed exploits the benefits of both the approaches. The radioactive source is used to initially calibrate the system, while the heating source is used to stabilize it during the data tacking. In particular, the heater pulses are used to monitor the bolometer gain as a function of its operating temperature, measured from the detector baseline[1]. With this procedure, the amplitude of each pulse is rescaled as a function of its baseline, allowing to compensate for the temperature thermal drift and to maintain the energy resolution at its optimum value for the entire data taking. The efficacy of such method has already been demonstrated in the CUORICINO[2] experiment, where a high-stability pulse generator has been used[3, 4].

In this paper we present a novel, multi-channel, ultra-stable and ultra-precise electronic system designed for the stabilization of the bolometer response. This new equipment is currently used in the CUORE[5, 6], LUCIFER[7], CUPID-0[8] and COSINUS[9] experiments, all located at the underground Laboratori Nazionali del Gran Sasso, Italy. In Sect.2 the description of the circuit is provided. In order to ensure high energy resolution and stability, particular care was addressed to ensure low noise and to minimize the thermal drift with respect to the operating temperature. The thermal calibration of the circuit and the performance in term of stability are shown in Sect.4. The results achieved concerning the pulse accuracy, spoiled by the jitter and electrical noise, are presented in Sect.5. The device can also been used to optimize the cryogenic temperature of operation of the bolometers and stabilize it against slow drifts. In Sect.6, a

detailed description of such architecture and the results achieved in the experimental context will be shown.

## 2 Circuit description

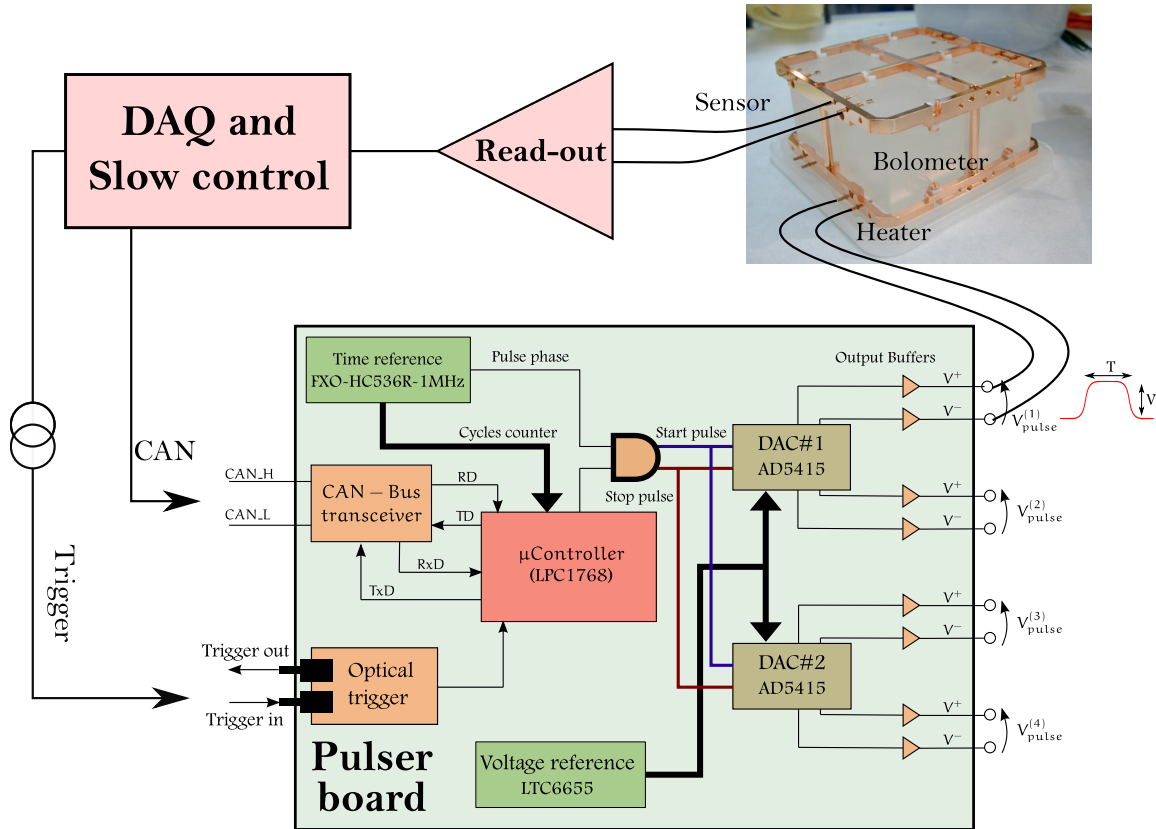


Figure 1: Simplified scheme proposed to calibrate the bolometer response.

The pulser board has been specifically designed to provide calibrating pulse with an outstanding stability, extremely low noise and timing precision, large flexibility, high reliability and two input/output optical converters to receive an optional external trigger and share it in a daisy chain configuration. Each board has 4 four output channels able to independently provide squared calibrating pulses.

The device consists of a four layer Printed Board Circuit hosting a Cortex M3 LPC1768, 32-bit micro-controller from NXP, managing all the on-board peripherals. The micro-controller communicates to the remote control system through a 100 kbit/s CAN bus. In such industrial protocol each command is preceded by a 11/29 bit code which uniquely identifies the desired board, shearing the bus with all the others. Thus, a single link is enough to connect all the needed boards, minimizing the cabling budget. Moreover, a very high reliability is guaranteed by the fact that each node on the bus actively contributes to detect eventual communication errors and correct for them.

Figure 1 shows the main blocks composing the pulse generation chain for a typical application such as the CUORE experiment. The high precision square pulse is driven inside the cryostat by twisted connections and reaches the heater resistors glued on the bolometers. The power injected induces an increase of the temperature of the bolometer, according to Eq.1:

$$E[eV] = \eta \frac{V_0^2 T}{e R \varepsilon^2} \quad (1)$$

where  $\eta$  is the thermal coupling between the crystal and the heater,  $R$  is the resistor value,  $V_0$  and  $T$  the pulse differential amplitude and width,  $\varepsilon$  the attenuation factor due to the output voltage divider (as explained below) and  $e$  the electron charge. The energy released to the bolometer is converted into a voltage signal by the thermal sensor (such as a Neutron Transmutation Doping thermistor, in the case of CUORE and CUPID-0 experiments), amplified by the front-end electronics and digitalized by the DAQ system.

In order to easily tag the calibrating pulse and prevent synchronization issues, it is convenient that the DAQ system triggers the pulse delivery instead of the slow control system, responsible to set the pulse parameters. In particular, the DAQ provides a digital TTL transition which is converted to an optical pulse, driven to the pulser board front panel, hosting an optical receiver triggering the pulse generation. The trigger is provided by an optical signal in order to completely decouple the noisy DAQ system to the sensitive pulser board. The optical trigger can also be daisy chained among all the desired boards, so that a unique optical connection from the DAQ system to the pulsers is enough to provide the trigger to the whole system. This is particular handy as the pulser boards are usually located far from the DAQ system, close to the cryostat and possibly inside a Faraday cage.

Figure 1 also exhibits the main blocks used to generate the calibrating pulse. In order to obtain precise pulse transitions, the pulser board is equipped with the FXO-HC536R oscillator, a very accurate device able to provide a 1 MHz reference clock with a declared phase stability of  $\pm 25$  ppm. This time reference is connected at the input of the LPC1768 micro-controller which can enable or disable the clock source and count its cycles. The first order estimation of the pulse width is obtained simply by converting the desired duration in terms of equivalent clock cycles (i.e. as an integer multiple of the 1  $\mu$ s time unit). However, the timing performance of the micro-controller is not good enough to directly trigger the pulse transitions. Instead, the voltage generator is triggered by a fast flip-flop (the NC7SV74 from Fairchild Semiconductor) connected to both the micro-controller and the reference oscillator. The micro-controller acts as a gate: when the gate is closed, the flip-flops maintain the output voltage generator in reset mode. The gate is opened as soon as the micro-controller clock cycles counter matches with the target value (i.e. the pulse coarsely lasts as desired). Being the gate opened, the flip-flop triggers the pulse transitions at the first reference clock rising edge. Using such architecture, the timing performance only depends on the precise clock reference and the fast flip-flop performance. In particular, the phase stability of the generated pulse coincides to that of the reference clock irrespectively to the pulse width and the micro-controller response. The outcomes of the timing performance characterization in term of temperature stability and random fluctuations will be shown in Sect.4 and Sect.5 respectively. Finally note that the boards is equipped with two more clocks which serves as reference for the micro-controller operation and for the on-board Analog-to-

Digital (ADC) converter. In order to prevent that the fast transitions of the clocks could introduce high frequency disturbances induced by the associated electromagnetic field, all these noisy components are enclosed inside a grounded metallic box acted as a local Faraday cage shields.

The output voltage generator system is based on the very precise and low noise voltage reference LTC6655, from Linear Technology. This component generates a 5 V voltage reference ensuring a high thermal stability (few ppm/°C) and a negligible sensitivity to the humidity level if packaged in the LS8 hermetic case. In order to reduce its noise contribution by a factor of 30%, two components are connected in parallel and averaged, so that the resultant value is used to feed the AD5415, a 12-bit, dual channel Digital-to-Analog converter (DAC), from Analog Devices. Coupled with the low noise and high precision OPA140 operational amplifier, from Texas Instrument, the DAC can be schematized as a settable resistor, ranging from 10 kΩ to an open circuit, as shown in Fig.2.

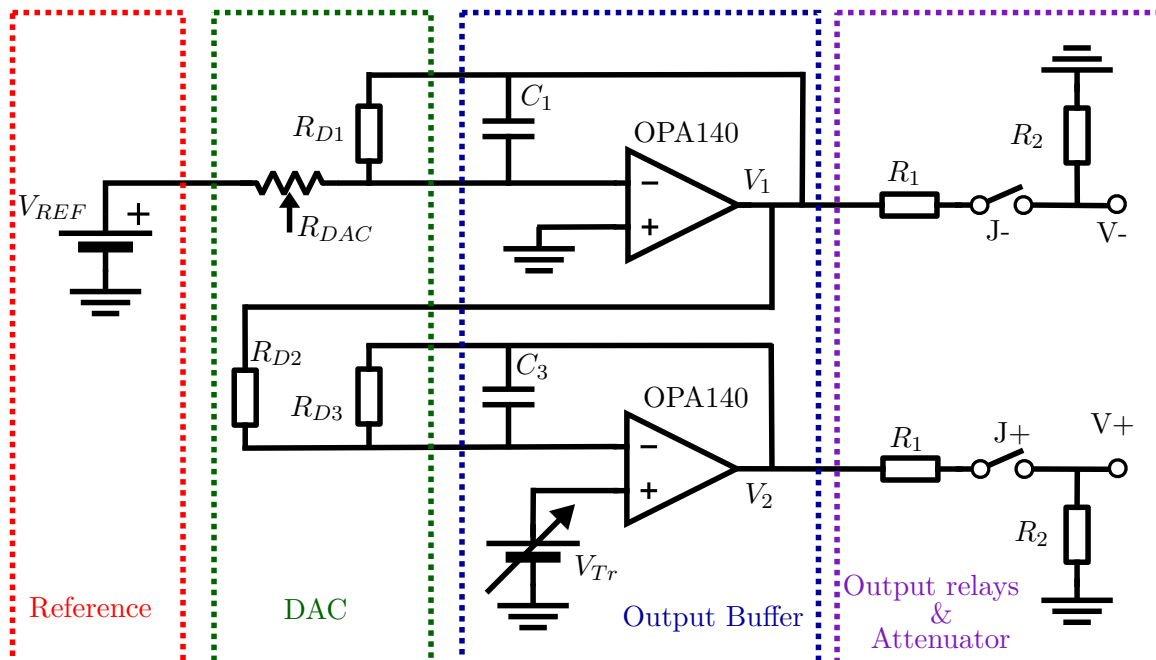


Figure 2: Simplified schematic of a pulser board channel

Since  $R_{D1}$  amounts to 10 kΩ and the OPA140 is used in inverting configuration, this architecture deliver a negative voltage level ranging from ground to  $-V_{REF} = -5$  V. This signal is also driven at the input of a second inverting unity gain amplifier, composed of a second OPA140 operational amplifier and the  $R_{D2} = R_{D3} = 20$  kΩ resistors embedded in the DAC. As a result, a differential signal up to 10 V can be supplied between the outputs. Capacitors  $C_1$  and  $C_3$  limits the bandwidth of the device to  $BW = 1.3$  MHz, in order to increase the output buffer phase margin and avoid ringing superimposed to the square pulse. Note that the positive terminal of the second

inverting amplifier is not referred to ground but to a settable voltage ( $V_{Tr}$ ), controlled by a 8-bit potentiometer. As shown in Sect.4.0.2, this component can add a proper offset at the positive node to compensate for offsets or thermal drifts of the voltage generation chain. An output ultra-stable voltage divider attenuates the differential signal by a factor of  $\varepsilon = R_2/(R_1 + R_2)$ , down to an energy range that fits the experimental needs (typically from few keV to several MeV). In most applications, where a heater resistor of few tens of k $\Omega$  is glued on the bolometer crystal, a typical attenuating factor of  $\varepsilon = 1/201$  is needed and accomplished by using  $R_1 = 5$  k $\Omega$  and  $R_2 = 25$   $\Omega$  ultra-stable resistor, from VISHAY FOIL RESISTORS. As a result, the pulse differential amplitude is given by Eq.2:

$$V_+ - V_- = \frac{V_0}{\varepsilon} = \frac{2}{\varepsilon} \left( \frac{R_{D1}}{R_{DAC}} V_{REF} + V_{Tr} \right) \quad (2)$$

The differential voltage can be connected to the heater by a dual channel bistable relay (the TQ2-L2, from Panasonic). In Sect.3 the design choice of the output voltage divider and its performance in term of thermal stability are shown in details. Each of the two channels of the DAC is connected to two independent output stages, so that 4 channels are available in total.

### 3 Output stage

The pulser board output stage is composed of an attenuator circuit and a coil latching bistable relay pair. The relays connect the pulser to the heater only during the pulse delivery, thus preventing that any electrical noise or disturbance can cause power injection towards the bolometers. The attenuating circuit consists of a classic voltage divider, which adjusts the signal range from the DAC by more than two order of magnitudes, to fit the energy range of interest of the experiments (typically in the keV/MeV domain). The voltage divider, made by ultra-stable and high precision resistor, from VISHAY FOIL RESISTORS, attenuates by a factor defined in equation 3:

$$\varepsilon = \frac{V_+ - V_-}{V_2 - V_1} = \frac{R_1 + R_2}{R_2} \quad (3)$$

Particular care must be devoted to design this block as any drift in the attenuating factor would deteriorate the performance of the overall device. Moreover, any disturbance picked up after the attenuation would remarkably deteriorate the energy resolution, as it would be superimposed to a much smaller signal.

The relay on-resistance contributes to compose  $R_1$ . In case of using MOSFET relay, although its series resistance amounts only to few ohms, its typical poor thermal stability (several tenths of percentage per  $^{\circ}\text{C}$ ) is not negligible and may spoil the overall performance in term of thermal stability. This guided the choice of using coil latching relays, which ensure a much lower contact resistor of few tens of m $\Omega$  that can be totally neglected.

According to the manufacturer,  $R_1$  and  $R_2$  are quoted to ensure a typical thermal drift of  $\frac{\partial R}{R \partial T} = +0.05$  ppm/ $^{\circ}\text{C}$  in the temperature range of interest (20 $^{\circ}\text{C}$ –60 $^{\circ}\text{C}$ ) and a long term stability of 50 ppm. In addition, the thermal drift of the attenuating factor

is even smaller, as the contributions of the two resistors have opposite sign, as shown in Eq.4.

$$\begin{aligned}
\frac{d\varepsilon}{\varepsilon dT} &= \frac{\partial\varepsilon}{\partial R_1} \frac{\partial R_1}{R_1 \partial T} \frac{R_1}{\varepsilon} + \frac{\partial\varepsilon}{\partial R_2} \frac{\partial R_2}{R_2 \partial T} \frac{R_2}{\varepsilon} \\
&= \frac{R_1}{R_1 + R_2} \left( \frac{\partial R_1}{R_1 \partial T} - \frac{\partial R_2}{R_2 \partial T} \right) \\
&\ll \frac{\partial R_1}{R_1 \partial T} \sim 5 \cdot 10^{-2} \text{ ppm}/^\circ\text{C}
\end{aligned} \tag{4}$$

As a result, the thermal drift of the attenuating factor is negligible. The resistor  $R_2$  is located downstream the relay, so that the heaters is referred to ground irrespective the relay status.

The drawback of using such kind of relays is that some disturbances can be induced at the nearby outputs by the magnetic energy released by the coil during the relay transition. Particular care must be therefore addressed to the circuit design and PCB layout in order to minimize the disturbances picked up from the magnetic flux variation. For instance, the same attenuating factor could have been obtained by locating a single ultra-stable resistor  $R = 2R_2$  across the outputs and using larger and inexpensive to refer each node to ground when the relays are opened. At a first glance, this solution would appear promising and cheaper than that used. Nonetheless, a coil with a total resistance of  $R+2R_2$  would be present at the output and capable to pick up magnetic flux variation. In particular, high frequency electromagnetic field due to relays transitions, clocks or environmental interference (wireless network or wi-fi, for instance, which works in the GHz domain) are extremely deleterious as they can induce large flux variation even in the small area output coil. The noise picked up cannot be filtered but it is driven to the heaters producing a heating proportional to the RMS voltage noise amplitude. This effect would be the most critical factor affecting the stability and the energy resolution of the whole system. Conversely, the use of two voltage dividers for each outputs, placed close to each other, with minimal area and proper relative orientation, would compose a pair of coils picking up a similar noise on both outputs. The power of such signal is consumed to ground through  $R_2$  as it acts as common mode signal across the heater. As a result, the symmetric solution proposed in Fig.2 turns out to be extremely effective in reducing the thermal power injection due to noise towards the bolometers.

## 4 Thermal stability

The thermal drift is the most important parameter that has to be taken into account to ensure the pulser stability. For example, the CUORE Faraday cage[?] hosting the pulser boards is not equipped with any thermalizing system in order to avoid the injection of low frequency disturbances. As a consequence, slow temperature drifts are expected in the experimental operation so that the pulser operation should be insensitive to them. According to Eq.1 and Eq.2, three pulser parameters plays an important role in the stability of the energy delivered: the pulse width ( $T$ ), dependent on the on-board reference oscillator, the voltage level produced at the DAC output ( $V_0$ ) and the attenuation factor of the output divider ( $\varepsilon$ ). In particular, the energy drift with respect

to the temperature variation is given by Eq.5.

$$\frac{dE}{EdK} = 2 \frac{\partial V_0}{V_0 \partial K} + \frac{\partial T}{T \partial K} - 2 \frac{\partial \varepsilon}{\varepsilon \partial K} \quad (5)$$

where  $K$  is the operating temperature. As described in Sect.3, the thermal drift of the voltage divider is completely negligible ( $\frac{\partial \varepsilon}{\varepsilon \partial K} \sim 5 \cdot 10^{-2}$  ppm/ $^{\circ}\text{C}$ ). The contribution of the pulse width and amplitude to the stability of the energy delivered are presented in Sect.4.0.1 and Sect.4.0.2, respectively. Each pulser board undergo a thermal calibration procedure to mitigate the thermal drifts so that  $\frac{dE}{EdK} \sim 0.1$  ppm/ $^{\circ}\text{C}$  is achieved in a temperature range going from 20 $^{\circ}\text{C}$  up to 60 $^{\circ}\text{C}$ . The method developed to enhance the thermal stability and the obtained results will be shown in Sect.4.0.3.

#### 4.0.1 Pulse width stability

The pulse width depends on the performance of the FXO-HC536R reference oscillator. In particular, if the clock period changes as a function of the operating temperature, then the pulse energy drifts proportionally. The pulse width thermal drift was measured using a Rohde&Schwarz RTO1044 oscilloscope (vertical resolution of 14-bits, 100 MHz bandwidth, time resolution of few tens of picoseconds, dependent on the pulse width), kept at room temperature, while the board under test operates in climatic chamber which increases the operating temperature from 20 $^{\circ}\text{C}$  to 60 $^{\circ}\text{C}$ , with a constant slope of 0.1 $^{\circ}\text{C}$  per minute. Such slow temperature variation ensures that the pulser board is in thermal equilibrium with respect to the environment during all the measurement. Every 5 $^{\circ}\text{C}$ , a series of pulses ( $V_0 = 5$  V,  $T = 1$  ms,  $\varepsilon = 1$ ) were delivered by the pulser under test. The oscilloscope acquires both positive and negative outputs, calculates the differential signal and measures the pulse width from the delay between the points where the differential signal crosses a threshold placed at half of the pulse amplitude on the rising and falling edges. For each temperature of interest, 10<sup>3</sup> identical pulses are provided and the measured pulse widths are collected into a histogram and fitted with a Gaussian function, as shown in Fig.3.a. The pulse width as a function of the temperature can be obtained as the mean value of the Gaussian fit for each sequence of pulses. The typical pulse width thermal drift is shown in Fig.3.b.

The outcomes show that the pulse width slightly increases with the temperature. The clock thermal drift is almost linear, with a typical slope of 0.3 – 0.4 ppm/ $^{\circ}\text{C}$ . Only small deviation from this trend was observed at the highest temperatures ( $K \geq 50^{\circ}\text{C}$ ). The slope of the pulse width with respect to the temperature is measured for each device, stored in the on-board EEPROM and used to properly compensate the pulse amplitude.

#### 4.0.2 Voltage stability

Voltage drifts due to the operating temperature variations can be ascribed to several causes, following listed.

- **Voltage reference stability:** the voltage provided by the LTC6655 regulator changes with respect to the component temperature. This drift is component dependent, non linear and generally shows a minimum drift around  $K \sim 35^{\circ}\text{C}$ . The manufacturer quotes the voltage regulator thermal drift to  $\pm 2$  ppm/ $^{\circ}\text{C}$ . As,

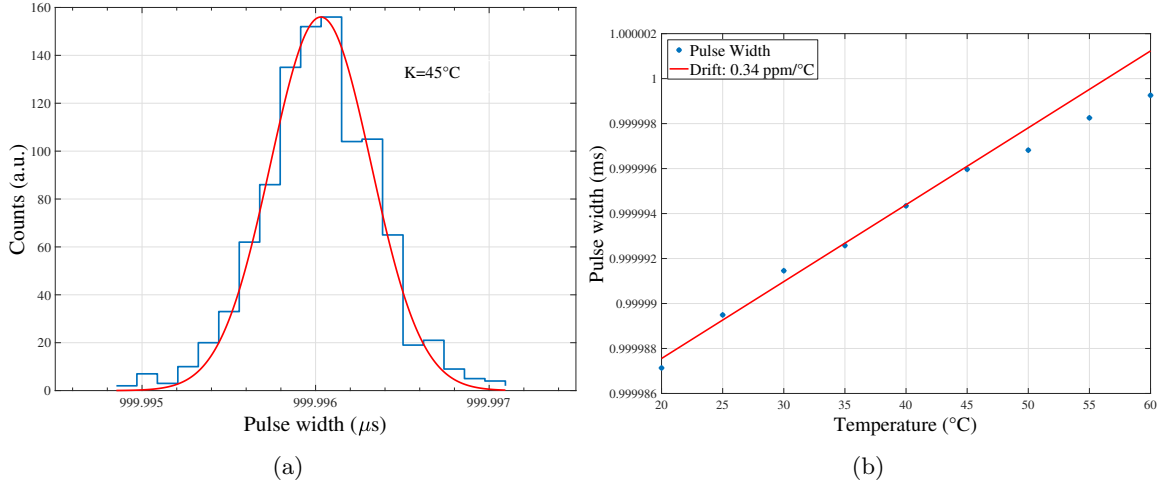


Figure 3: Pulse width thermal stability: on the left, the pulse width distribution acquired at  $45^{\circ}\text{C}$ . The average pulse width is given from the Gaussian center. On the right, the pulse width with respect to the temperature. The typical pulse width drift amounts to  $0.3 - 0.4$  ppm/ $^{\circ}\text{C}$ .

for low output signals, only a small fraction of the reference voltage is led at the outputs by the DAC, then the thermal drift of the LTC6655 dominates at larger amplitudes.

- **DAC stability:** the DAC response depends on the operating temperature in a complex and non linear way. The DAC gain variation with respect to the temperature is quoted to be  $\pm 5$  ppm/ $^{\circ}\text{C}$ , full range scale. These effects dominates the overall voltage instability for small output signals.
- **Thermal hysteresis:** the thermal drift of the voltage reference is not only proportional to the actual temperature, but also depends on whether the temperature is increasing or decreasing. This phenomenon is called thermal hysteresis and is particularly deleterious in case of fast temperature changes. In worse case condition, the thermal hysteresis might result in an instability of the order of 30 ppm. Even if the experimental environment is not equipped with an active system to keep the operating temperature stable, the temperature is expected to slowly change during the data taking, thus mitigating the hysteresis effects.
- **Mechanical strains:** temperature increase causes the expansion of all the metals composing the pulser board. Large ground or power supply planes are particularly affected by such effect. The mechanical stress caused by the pins soldered to an expanding printed circuit board may cause the output voltage provided by the voltage reference to variate. Proper layout technique significantly reduces the stress on this integrated circuit and helps to mitigate this second order effect.
- **Humidity:** with changes in relative humidity, plastic packaging materials absorb water and change the amount of pressure they apply to the die inside. Considering the voltage reference, this strain can cause slight changes in the output of a voltage reference, usually of the order few tens of ppm. To prevent such effect,

the voltage reference is packaged in the hermetic LS8 enclosure, so that humidity negligibly contribute to the drift. Residual second order effects can be ascribed to the mechanical stress applied to the voltage reference by the printed circuit board material which may absorb water.

- **Long-term drift:** this non thermal dependent effect describes voltage reference shows a variation as a function of the operational time. Long-term drift cannot be extrapolated from accelerated high temperature testing since this erroneous technique gives drift numbers that are wildly optimistic. The only way long-term drift can be determined is to measure it over the time interval of interest, preventing us to measure and compensate for this effect. To mitigate it, the pulser board is equipped with voltage reference in LS8 package, whose long-term drift is quoted to be  $\pm 20$  ppm/ $\sqrt{\text{kHr}}$ . Since this effect is proportional to the square-root of the time, its contribution becomes smaller after long period of operation. In addition, the periodic calibration with radioactive sources planned during an experiment lifetime are useful to compensate this second order effect.

The voltage drift as a function of temperature has been measured placing the pulser board in the VOTSCH VT-7004 climatic chamber. The environment temperature is increased linearly from 20°C to 60°C, with a slope of 0.1°C per minute. During the temperature cycle, the remote control makes each pulser channel generate a static voltage level (from 1 V to 10 V, 1 V step), measured with the 3706A Multimeter, from Keithley, kept at room temperature. Such multimeter is able to measure with extremely high accuracy and stability the voltage delivered from the pulser board, so that even small drifts can be observed.

Figure 4 (blue curves) shows the measured thermal drift as a function of the temperature. The drift behaviour significantly changes as a function of the amplitude delivered. In particular, at lower amplitudes (Fig.4.a) the contribution of the voltage reference is largely attenuated and the DAC thermal drift dominates the overall instability. On the other hand, at larger output amplitudes (Fig.4.b) the plot changes since the relative contribution of the voltage reference increases while the DAC contribution does not change. In this condition the voltage shows a negative slope below  $\sim 35^\circ\text{C}$ , while a positive drift at larger temperatures. The typical voltage drift order of magnitude amounts to several ppm/°C.

### 4.0.3 Total drift

Although the thermal drift depends on a lot of different effects combined in complex and non linear way, the intrinsic pulse energy stability is of the order of several part per million per Celsius degree, as previously descibed. Nevertheless, most of the residual thermal drift can be compensated by injecting a correcting voltage level ( $V_{tr}$ ) into the positive output buffer (see Fig.2 and Eq.2). This voltage can be adjusted with a resolution of  $\sim \mu\text{V}$  by managing the on-board 8-bit AD5263 digital potentiometer, from Analog Devices. Given the complex dependence of pulse energy from temperature, the drifts must be empirically measured on each board to be compensated. Before undergoing the thermal calibration, each board is kept turned on for two days at controlled temperature to mitigate the long-term drift contribution. During this period, the digital potentiometer is calibrated and its average step is recorded in the on-board EEPROM. Moreover the pulser baseline is measured and the potentiometer is initially set to com-

penstate for the output offset. Baseline offsets lower than  $1 \mu\text{V}$  are achieved. After that, the clock thermal drift is measured for each board in the temperature range from  $20^\circ\text{C}$  to  $60^\circ\text{C}$ . The pulse width drift is assumed to be linear and the slope coefficient is measured and store in the pulser EEPROM memory (see Fig.3.b). Such value is used to properly under-compensate the pulse amplitude in order to correct for the clock thermal drift. Finally, the voltage thermal drift is measured as explained in Sect.4.0.2 in the temperature range from  $20^\circ\text{C}$  to  $60^\circ\text{C}$ , for output levels ranging from  $1 \text{ V}$  to  $10 \text{ V}$ ,  $1 \text{ V}$  step. For each amplitude level, the output voltage drift is measured every  $5^\circ\text{C}$ . Within these intervals the drift is assumed to be linear so that the compensating factor can be extrapolated as a function of the temperature and the desired pulse amplitude. The boards are also equipped with two diodes which make them able to measure the actual operating temperature from the direct voltage drop of a PN-junction (which typically decreases linearly by  $\sim -2 \text{ mV}/^\circ\text{C}$ .) Besides the output drift, also the diodes are calibrated so that the operating temperature can be estimated with a precision of  $\sim 1^\circ\text{C}$  by reading the forward voltage drop by means of the on-board ADC.

After the calibration, the pulser board measures the actual temperature before the pulse delivery and sets a proper correcting voltage  $V_{tr}$  given by Eq.6:

$$V_{tr} = - \left[ 2 \frac{\partial V_0}{V_0 \partial K} \Big|_{K_\alpha} + \frac{\partial T}{T \partial K} \Big|_{K_\alpha} \right] \quad (6)$$

where  $K_\alpha$  is the actual temperature. All the factors are known from the calibration procedure.

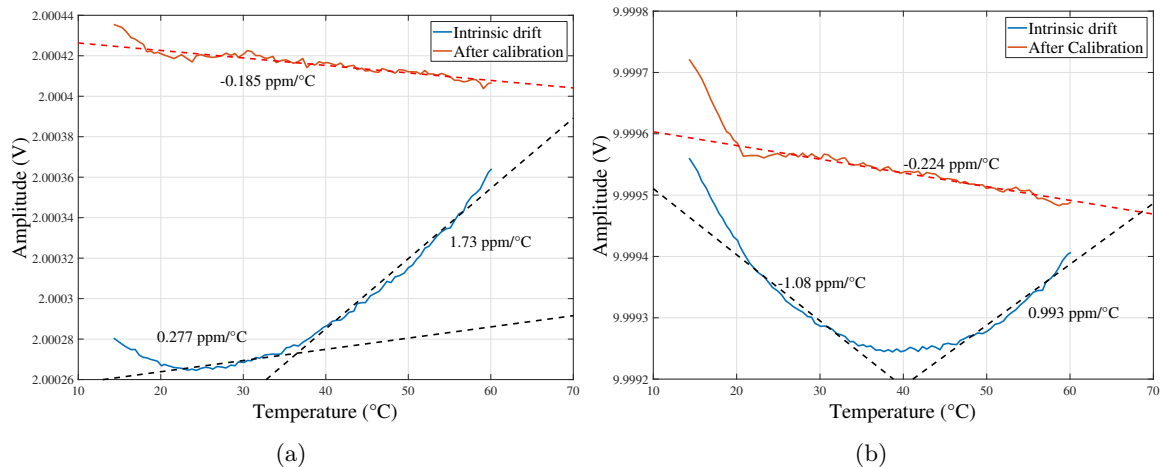


Figure 4: Intrinsic (non-compensated) and corrected (compensated) pulse amplitude thermal drift, in blue and orange respectively. The plot are shown for low (2 V, on the left) and high amplitudes (10 V, on the right). The drift is properly over-compensated to correct for the pulse width instability.

Figure 4 superimposes the intrinsic and compensated voltage thermal drift obtained for both low (Fig.4.a) or high (Fig.4.b) output levels. Note that the voltage drifts is deliberately under-compensated, so that the effect of linear and positive pulse width

thermal drift coefficient is also compensated. As expected, the thermal compensation is effective in the temperature range from 20°C to 60°C. The vertical separation between the two curves is adjusted to compensate for any initial offset so to keep the zero-amplitude level as close as possible to the ground reference.

The calibration procedure allows to reduce the thermal drift of the pulse energy by an order of magnitude, i.e. at the level of  $\sim 0.1$  ppm/°C. Figure 5 shows the residual thermal drifts for a batch of 46 devices. Since the contribution of the voltage reference changes its polarity around 35-40°C, the intrinsic thermal drift coefficient distribution is shown considering separately the results obtained at lower or higher temperature range. As it can be observed, the intrinsic thermal drift coefficient is  $\sim \pm 5 - 6$  ppm/°C. As shown in Fig.5.b, the residual thermal drift coefficient is  $\sim \pm 0.1$  ppm/°C, more than an order of magnitude lower than the performance measured before the calibration.

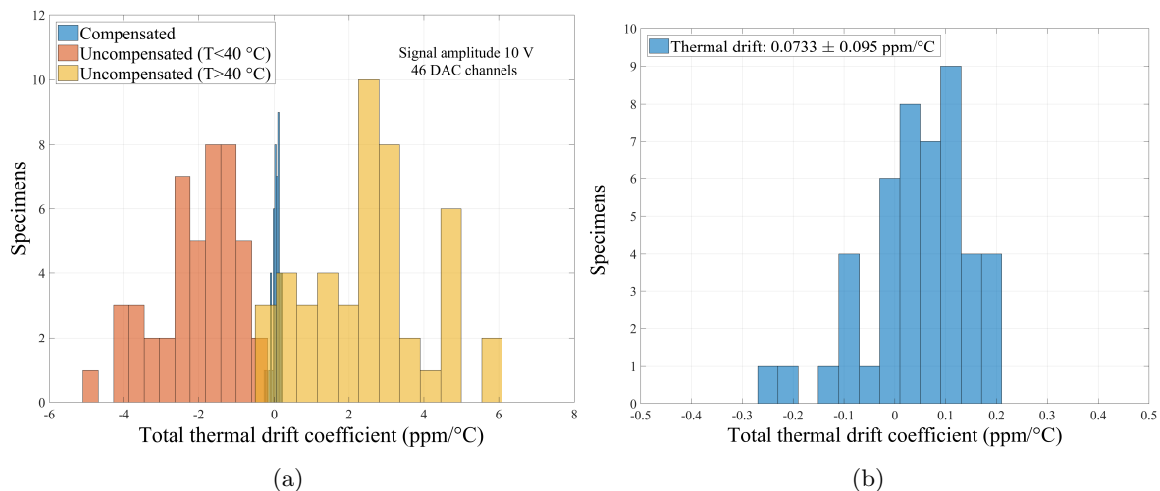


Figure 5: Efficacy of the thermal drift correction on the whole pulser board lot. Plot (a) shows the superposition of the intrinsic thermal drift distribution at low ( $T < 40^\circ\text{C}$ , orange histogram) and high temperature ( $T > 40^\circ\text{C}$ , yellow histogram). The blue histogram is the residual thermal drift distribution of the same board after performing the thermal drift compensation. Plot (b) shows the same result for the compensated board. The residual drift is off the order of 0.1 ppm/°C.

## 5 Pulse accuracy

Beside the calibrating pulse stability, the pulser must maximize the reproducibility of the calibrating pulses. Indeed, considering a sequence of identical pulses, any amplitude or width fluctuation with respect to their nominal value would result in a random variation of the energy delivered to the bolometers and, consequently, in the deterioration of the energy resolution of the calibrating peak in the acquired energy spectrum. In principle, this effect can be mitigated by sending a large number of calibrating pulses and taking the average energy provided by each pulse. However, a similar procedure is clearly

troublesome and, for practical reasons, cannot be pursued in a large scale experiments. On the other hand, if the fluctuation of the energy supplied by identical calibrating pulses is much lower than the intrinsic bolometer resolution (few keV), then the the pulser board negligibly contribute to the final peak energy resolution.

Concerning the contribution of the pulser board, the fluctuation of the delivered energy is due to the stochastic variation of the pulse amplitude or width, as expressed by Eq.7.

$$\left(\frac{\sigma_E}{E}\right)^2 = \left(\frac{\sigma_E}{E}\right)_{V_0}^2 + \left(\frac{\sigma_E}{E}\right)_T^2 \quad (7)$$

The contribution of these two sources of uncertainty will be studied separately in the next sections. As it will be described, the contribution of the electrical noise is the most critical factor spoiling the overall energy resolution, while the fluctuation of the pulse width is negligible. In particular, it will be shown that  $\sigma_E/E \sim (\sigma_E/E)_{V_0} \sim 10^{-2}/\sqrt{E[\text{eV}]}$ , whatever combination of T and  $V_0$  is used.

### 5.0.1 Electric noise effects

The main source of energy fluctuation can be ascribed to the electric noise of the pulser board which generates random additional power heating the bolometers. Figure 6 shows the most important sources of noise that have to be taken into account.

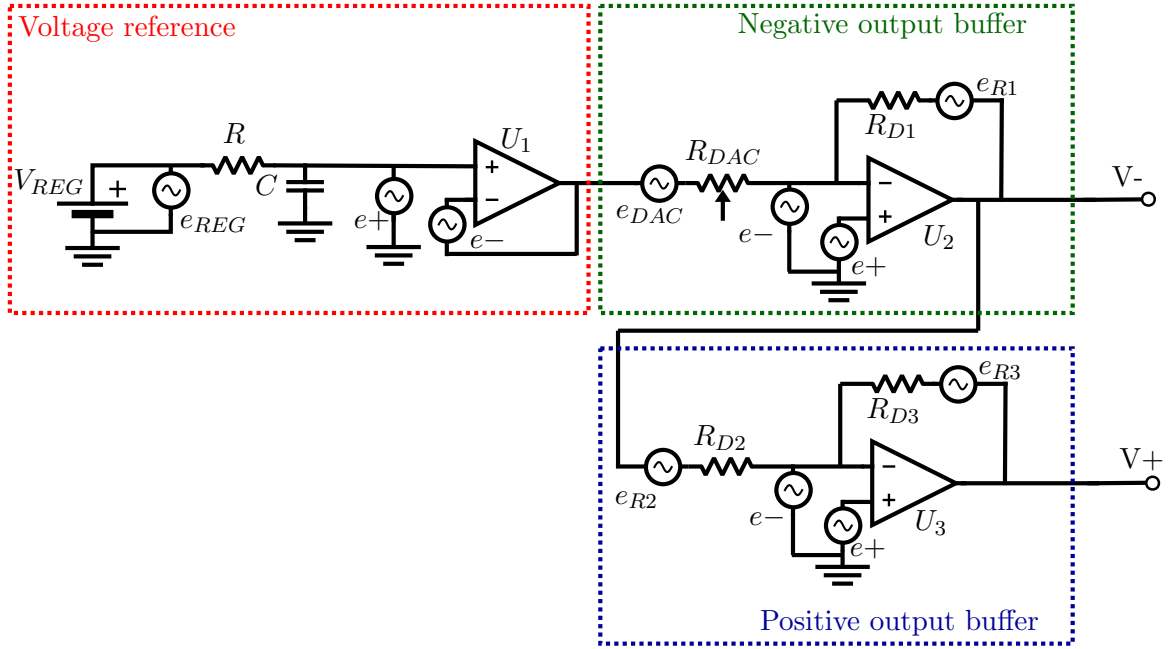


Figure 6: Simplified schematic of a pulser board channel. The most important noise sources are pointed out.

The first contribution is due to the 5 V reference regulator ( $e_{REG}$ ) and the low noise, high precision, OPA140 operational amplifier ( $U_1$ ) buffering this reference value ( $e_{\pm}$ ).

As mentioned, two LTC6655 linear regulator are used in parallel in order to reduce their noise contribution by  $\sim 30\%$ , so that  $e_{REG} \sim 60 \text{ nV}/\sqrt{\text{Hz}}$ . The reference voltage is filter by a RC low-pass filter ( $R = 50 \text{ } \Omega$ ,  $C = 10 \text{ } \mu\text{F}$ , cut-off frequency  $f \sim 300 \text{ Hz}$ ) which makes the reference white noise negligible over few hundreds Hz. Above the cutoff frequency, the noise figure is dominated by the buffer contribution ( $e_+ = e_- = 5 \text{ nV}/\sqrt{\text{Hz}}$ ). At the negative output, the noise of the reference block ( $e_{REF}$ ) depends on the  $R_{DAC}$  adjustable resistor (from  $10 \text{ k}\Omega$  up to an open circuit) or, equivalently, to the output voltage level  $V_-$ , as shown in Eq.8.

$$e_{REF}\Big|_{V_-} = \begin{cases} \frac{|V_-|}{V_{REG}} \sqrt{e_+^2 + e_-^2 + e_{REG}^2} = 0 - 60 \text{ nV}/\sqrt{\text{Hz}} & \text{if } f \ll 300 \text{ Hz} \\ \frac{|V_-|}{V_{REG}} \sqrt{e_+^2 + e_-^2} = 0 - 7 \text{ nV}/\sqrt{\text{Hz}} & \text{if } f \gg 300 \text{ Hz} \end{cases} \quad (8)$$

The second noise contribution is ascribed to the negative output buffer stage, due to the Johnson noise of the  $R_{DAC}$  and  $R_{D1} = 10 \text{ k}\Omega$  resistors and the input series noise of the OPA140 operational amplifier  $U_2$ . At  $V_-$ , the negative output buffer noise ( $e_{B_-}$ ) at room temperature, dependent on the output voltage, is given by Eq.9.

$$e_{B_-}\Big|_{V_-} = \frac{|V_-|}{V_{REG}} e_{DAC} + e_{R1} + \left( \frac{|V_-|}{V_{REG}} + 1 \right) \sqrt{e_+^2 + e_-^2} = 14 - 22 \frac{\text{nV}}{\sqrt{\text{Hz}}} \quad (9)$$

Since the noise contributions of the voltage reference and the negative buffer blocks are uncorrelated, the total expected noise at the output is given by the  $e_{V_-} = \sqrt{e_{REF}^2 + e_{B_-}^2}$ , given from Eq.9 and Eq.8. As well as the signal, the noise at the negative output is injected at the input of the inverting positive output buffer stage. In addition, the positive output buffer stage contributes to the total noise with the Johnson noise of the  $R_{D2} = R_{D3} = 20 \text{ k}\Omega$  resistors and the input series noise of the OPA140 operational amplifier  $U_3$ . Omitting the amplitude-dependent contribution coming from the negative output, the positive output buffer noise ( $e_{B_+}$ ) at room temperature referred to the positive output is given by Eq.10.

$$e_{B_+}\Big|_{V_+} = \sqrt{e_{R2}^2 + e_{R3}^2 + 8e_+^2} = 29 \frac{\text{nV}}{\sqrt{\text{Hz}}} \quad (10)$$

Let us calculate the differential noise expected across the heating resistor. Since the negative output voltage is driven at the input of the inverting positive buffer stage and affects both output nodes, then its weight is doubled. On the other hand,  $e_{B_+}$  is an independent source of noise, so that it has to be quadratically summed to the variance of the negative node. The differential white noise across the heating resistor is finally described by Eq.11.

$$e_W = \sqrt{e_{B_+}^2 + 4(e_{REF}^2 + e_{B_-}^2)} = \begin{cases} 40 - 130 \text{ nV}/\sqrt{\text{Hz}} & \text{if } f \ll 300 \text{ Hz} \\ 40 - 55 \text{ nV}/\sqrt{\text{Hz}} & \text{if } f \gg 300 \text{ Hz} \end{cases} \quad (11)$$

The differential noise  $e_W$  was measured by amplifying it with a low noise OP27 operational amplifier (close-loop gain of  $20 \text{ V/V}$ ) and acquiring the final signal with an Agilent 4395A spectrum analyzer in the frequency range  $10 \text{ Hz} - 5 \text{ MHz}$ . The additional amplification stage, coupled in AC through a  $2200 \text{ } \mu\text{F}$  capacitor, is useful to increase the noise at the output of the pulser board with respect to that due to the spectrum analyzer and the OP27 amplifier. The acquired power noise spectrum referred to the

pulser output node can be easily calculated by dividing the outcomes by the close-loop gain. Figure 7.a shows the noise power spectra distribution measured at various output static values. Figure 7.b compares the expected and measured white noise pedestal as a function of the signal amplitude. The expectations are in good agreement with the measurement.

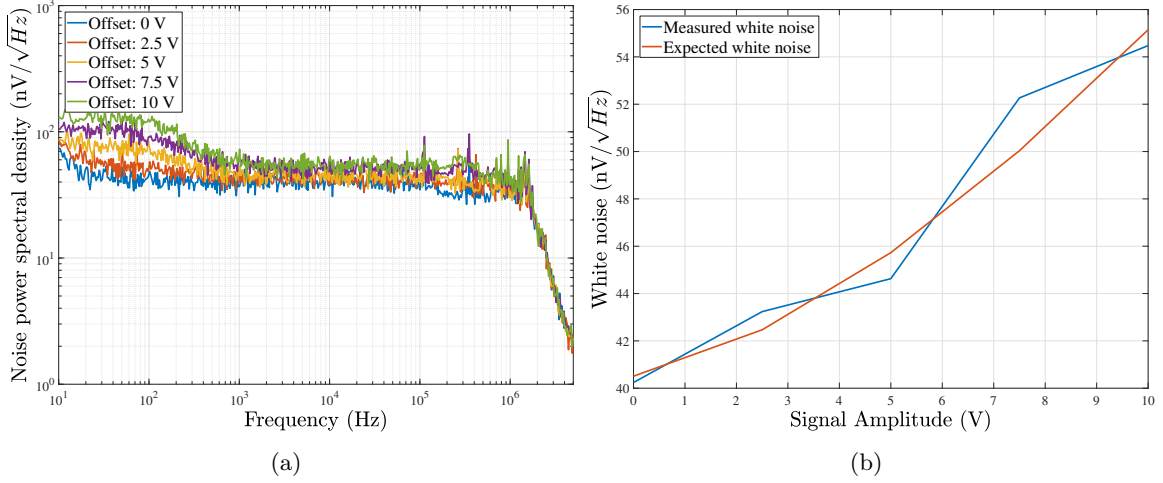


Figure 7: On the left, noise power spectra density at different amplitude measured from the difference between  $V_+$  and  $V_-$  terminals. On the right, the expected and measured white noise as a function of the signal amplitude.

Let us calculate how much power due to such noise contributes on average to the thermal power induced towards the bolometers. Using the same notation of Eq.1, providing a sequence of  $N$  identical square pulses, the mean energy delivered can be expressed as in Eq.12.

$$\begin{aligned}
 \overline{E[eV]} &= \frac{\eta}{eR\varepsilon^2} \lim_{K \rightarrow \infty} \frac{1}{K} \sum_{k=1}^K \int [V(t) + N_k(V, t)]^2 dt \\
 &= \frac{\eta}{eR\varepsilon^2} \lim_{K \rightarrow \infty} \frac{1}{K} \sum_{k=1}^K \left( \int_0^T V_0^2 dt + \int_0^T N_k^2(V_0, t) dt + 2 \int_0^{2\tau} N_k^2(0, t) dt + 2V_0 \int_0^T N_k(V_0, t) dt \right)
 \end{aligned} \tag{12}$$

where  $\tau \sim 5$  ms the period in which the relays are connected prior and after the pulse delivery and  $N_k$  the  $k$ -th time and amplitude dependent noise sample. The lower limits of integrations can be set to zero given that the noise is a stochastic stationary process. The first addend of Eq.12 represents the power injected by a noiseless ideal pulse. The second term represents the power due to the RMS noise during the pulse delivery, thus it must be calculated at  $V_0$  and integrated in time  $T$ . Similarly, the third term concerns the RMS contribution of the baseline noise (calculated at zero amplitude), whose power has to be integrated for  $2\tau$ , where the factor 2 considers both the periods before and after the pulse generation. By integrating the white noise of Eq.11 on the

device bandwidth ( $BW \sim 1.3$  MHz), one can estimate the RMS noise at the desired amplitude. In particular, since  $N_{\text{RMS}} = e_W \cdot \sqrt{BW} \sim 10^{-4} V_{\text{RMS}}$ , the contribution of the second and third terms of Eq.12 to the pulse energy is totally negligible as proportional to  $(N_{\text{RMS}}/V_0)^2 \sim 10^{-8}$ . Finally, the fourth term of Eq.12 represents the mean value of the noise, which is zero for long time integration or, equivalently, for  $K \rightarrow \infty$ . In conclusion, it proves that the mean energy delivered by the calibrating pulse is extremely close to that shown in Eq.1 (at the level of  $10^{-2}$  ppm).

The pulse energy fluctuation can be expressed as in Eq.13.

$$\begin{aligned} \sigma_E^2[eV] &= \lim_{K \rightarrow \infty} \frac{1}{K} \sum_{k=1}^K \left( \int \frac{\eta}{eR\varepsilon^2} [V(t) + N_k(V, t)]^2 dt - \bar{E} \right)^2 \\ &= 4V_0^2 \left( \frac{\eta}{eR\varepsilon^2} \right)^2 \lim_{K \rightarrow \infty} \frac{1}{K} \sum_{k=1}^K \left( \int_0^T N_k(V_0, t) dt \right)^2 \end{aligned} \quad (13)$$

The integral in Eq.13 can be calculated in the frequency domain, as shown in Eq.14.

$$\begin{aligned} \lim_{K \rightarrow \infty} \frac{1}{K} \sum_{k=1}^K \left( \int_0^T N_k(V_0, t) dt \right)^2 &= \lim_{K \rightarrow \infty} \frac{1}{K} \sum_{k=1}^K \left( \int_{-T/2}^{T/2} N_k(V_0, t) dt \right)^2 \\ &= \lim_{K \rightarrow \infty} \frac{1}{K} \sum_{k=1}^K \left[ \int_{-T/2}^{T/2} \left( \frac{1}{\pi} \int_0^{+\infty} N_k(V_0, \omega) e^{i\omega t} d\omega \right) dt \right]^2 \\ &= \lim_{K \rightarrow \infty} \frac{1}{K} \sum_{k=1}^K \left[ \frac{1}{\pi} \int_0^{+\infty} N_k(V_0, \omega) \left( \int_{-T/2}^{T/2} e^{i\omega t} dt \right) d\omega \right]^2 \\ &\sim \lim_{K \rightarrow \infty} \frac{1}{K} \sum_{k=1}^K N_k^2(V_0) \left[ \frac{1}{\pi} \int_0^{+\infty} \frac{2}{\omega} \sin\left(\frac{\omega T}{2}\right) d\omega \right]^2 \\ &= \overline{N_k^2}(V_0) = \frac{T}{2\pi BW} N_{\text{RMS}}^2(V_0) \sim \frac{T}{2\pi} e_W^2(V_0) \end{aligned} \quad (14)$$

where  $N_{\text{RMS}} \sim e_W^2 \cdot BW \sim 100 \mu\text{V}$  is the RMS noise. The first equivalence of Eq.14 exploits that the noise is a stationary stochastic process, while the last equations follows from the Parseval's theorem calculated on a ideal T-wide rectangular pulse. Note that Eq.14 approximates the noise figure to its white contribution ( $N_k(V_0, \omega) = N_k(V_0)$ , independently of the frequency). By substituting Eq.14 in Eq.13, one obtains:

$$\sigma_E^2[eV] = \left( \frac{\eta}{eR\varepsilon^2} \right)^2 \frac{4V_0^2 T e_W^2}{2\pi} = \frac{\eta}{eR\varepsilon^2} \frac{2e_W^2}{\pi} \bar{E} \quad (15)$$

Equation 15 states that  $(\sigma_E/\bar{E})^2 \propto \bar{E}^{-1}$ , thus the relative resolution is inversely proportional to the square root of the pulse energy and the signal to noise ratio increases at higher energies. Moreover, in this approximation, the pulse resolution does not depend on the pulse amplitude or width, whatever combination of  $V_0$  and  $T$  has been chosen. By replacing the typical values ( $\eta \sim 0.5$ ,  $R \sim 10$  k $\Omega$ ,  $\varepsilon \sim 200$ ,  $e = 1.6 \cdot 10^{-19}$  C and  $e_W \sim 50$  nV $\sqrt{\text{Hz}}$ ) in Eq.15, one obtains:

$$\frac{\sigma_E}{\bar{E}} \sim \frac{4 \cdot 10^{-3}}{\sqrt{\bar{E}}} \quad (16)$$

Equation 16 implies that the intrinsic resolution of a typical 1 MeV calibrating pulse amounts to 10 eV FWHM. This value must be compared to the energy resolution achieved by the detectors, which can be evaluated from the RMS fluctuation of their baselines. Typically, in experiments using macro-bolometers such as CUORE or CUPID-0, the target energy resolution is of the order of few keV FWHM, so that the contribution of the pulser board is totally negligible.

### 5.0.2 Time fluctuation effects

The time fluctuation  $\sigma T$  of the pulse width also contributes to deteriorate the resolution of the calibrating peak in the acquired energy spectrum. As mentioned in Sect.2, this signal is provided by the precise 1 MHz oscillator HC536R-1, from FXO Electronics, which feeds the fast NC7SV74K8X flip-flop from Fairchild Semiconductor. This architecture ensures both a very precise phase stability, only dependent on the oscillator performance, and fast rise and fall time transitions, limited by the output buffer stage bandwidth. Indeed, the output buffer bandwidth is set to  $BW \sim 1.3$  MHz in order to ensure high phase margin and low ringing during the pulse transitions.

The time fluctuation has been estimated by acquiring a sequence of 500 identical pulses with the Rohde&Schwarz RTO 1044 oscilloscope (4 GHz bandwidth, 10 GHz/Ch sample frequency,  $10^7$  samples per trigger, High Resolution mode with 14 equivalent bits of vertical resolution and bandwidth of 100 MHz). The acquiring window exceeded the pulse width and amplitude by 10%, in order to minimize the uncertainties related to the discrete sampling and the limited vertical resolution. The pulses can be triggered when crossing a settable threshold ( $V_\alpha$ ), equal to a desired fraction ( $\alpha$ ) of the pulse amplitude, so that  $\alpha = V_\alpha/V_0$ . The pulse width is measured as the time difference between when the rising and falling transitions cross half amplitude ( $\alpha = 0.5$ ). The observed time fluctuation  $\sigma_{T_O}$  is obtained as the standard deviation of the pulse width distribution.  $\sigma_{T_O}$  is due to two uncorrelated effects:

- $\sigma_{T_T}$  is directly referred to the uncertainties affecting the time dimension. The first contribution to be taken into account is the phase stability of the reference oscillator ( $\sigma_{T_p}$ ). According to the datasheet provided by the manufacturer, the HC536R-1 ensures a phase stability of  $\pm 25$  ppm with respect to the clock nominal frequency (1 MHz). The second contribution is the oscilloscope resolution on the horizontal axes (time scale). In particular, the finite record buffer length and the sample frequency limit the maximum sample frequency to the ratio between the acquiring window width and the memory buffer length. For instance, for pulse widths of  $T = 500$  ms, the oscilloscope time resolution is  $\sigma_{T_{osc}} = 55$  ps. Note that such uncertainties affect both transitions of the calibrating pulse, so that the total pulse width fluctuation is given by:

$$\sigma_{T_T} = \sqrt{2(\sigma_{T_p}^2 + \sigma_{T_{osc}}^2)} \sim 85 \text{ ps.} \quad (17)$$

- $\sigma_{T_N}$  is related to the electric noise and the finite bandwidth of the output buffer stage. The pulse width is evaluated from the time where the pulse crosses a fixed voltage threshold  $V_\alpha = V_0/2$ . If the transitions were ideally vertical (infinite pulser bandwidth), then the voltage noise would have not been able to affect the measurements. On the contrary, given a finite bandwidth, the trigger time fluctuates as a consequence of the vertical position uncertainty of the trigger point

due to the electric noise. This effect stochastically affects both rising ( $\sigma_{T_R}$ ) and falling ( $\sigma_{T_F}$ ) pulse edges, as expressed by Eq.18.

$$\sigma_{T_N}^2 = \sigma_{T_R}^2 \Big|_{\alpha} + \sigma_{T_F}^2 \Big|_{\alpha} = \left( \frac{dV_R}{dt} \right)^{-2} \Big|_{t_{\alpha}} \sigma_V^2 + \left( \frac{dV_F}{dt} \right)^{-2} \Big|_{t_{\alpha}} \sigma_V^2 \quad (18)$$

where  $t_{\alpha}$  is the trigger time at the trigger threshold and  $\sigma_V$  is the RMS noise at the oscilloscope input. For a finite bandwidth ( $BW = 1/2\pi\tau = 1.3$  MHz), the rising and falling edges can be expressed as:

$$\begin{aligned} V_R(t) &= V_0 (1 - e^{-t/\tau}) \\ V_F(t) &= V_0 e^{-t/\tau} \end{aligned} \quad (19)$$

with  $\tau \sim 250$  ns. By using Eq.19, one can solve Eq.18 and obtain:

$$\sigma_{T_N}^2 \Big|_{\alpha} = \left[ \frac{(1 - \alpha)^2 + \alpha^2}{(1 - \alpha)^2 \alpha^2} \right] \frac{\tau^2}{V_0^2} \sigma_V^2 \quad (20)$$

$\sigma_{T_N}^2 \Big|_{\alpha}$  has a minimum for  $\alpha = 0.5$ . In this case, Eq.20 becomes:

$$\sigma_{T_N}^2 \Big|_{\alpha=0.5} = 8 \frac{\tau^2}{V_0^2} \sigma_V^2 \quad (21)$$

As mentioned,  $\sigma_V^2$  is the RMS electrical noise read by the RTO 1044 oscilloscope. Thus:

$$\sigma_V^2 = \sigma_{V_{RMS}}^2 + \sigma_{V_{pre}}^2 + \sigma_{V_{dig}}^2 \quad (22)$$

where  $\sigma_{V_{RMS}} \sim 100$   $\mu$ V is the pulser RMS noise calculated over the output buffer full-bandwidth,  $\sigma_{V_{pre}}$  is the RMS noise if the oscilloscope analog front-end circuit and  $\sigma_{V_{dig}}$  is the RMS voltage resolution of the oscilloscope ADC. The two latter contributions are calculated over the full oscilloscope bandwidth (up to 100 MHz). Note that  $\sigma_{V_{RMS}}$  slightly increases with  $V_0$  (as shown in the previous section),  $\sigma_{V_{dig}} = \gamma V_0$  ( $\gamma \sim 400$   $\mu$ V/V, according to the manufacturer specs) since the equivalent voltage step of the less significant bit is proportional to the vertical scale set up to the oscilloscope, while  $\sigma_{V_{pre}}$  is independent of  $V_0$  so that its contribution becomes negligible with respect to  $\sigma_{V_{dig}}$  at large signal amplitudes.

$\sigma_{T_O}$  is given by the square root of the sum of the variance related to each of them. From Eq.17, Eq.21 and Eq.22 one obtains:

$$\begin{aligned} \sigma_{T_O}^2 &= \sigma_{T_T}^2 + \sigma_{T_N}^2 \Big|_{\alpha=0.5} \\ &= 2\sigma_{T_P}^2 + 2\sigma_{T_{osc}}^2 + \frac{8\tau^2}{V_0^2} \left( \sigma_{V_{RMS}}^2 + \sigma_{V_{pre}}^2 \right) + 8\tau^2\gamma^2 \end{aligned} \quad (23)$$

Equation 23 describes the jitter error experimentally measured at half of the pulse amplitude, univocally defined by  $\alpha = 0.5$ . The first and third terms are that due to the pulser board, while the other factors represent the setup sensitivity. Note that,  $\sigma_{T_O}$  decreases by increasing the signal amplitude and, neglecting all the contributions

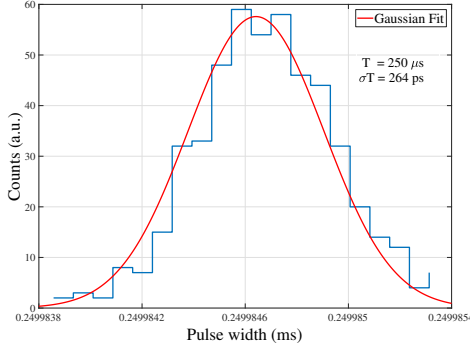


Figure 8: Pulse width distribution acquired recording 500 pulses, 10 V height, 250  $\mu\text{s}$  wide. In red, the Gaussian function fitting the distribution. The measured average pulse width and its fluctuation is given from the center and standard deviation of the fit result.

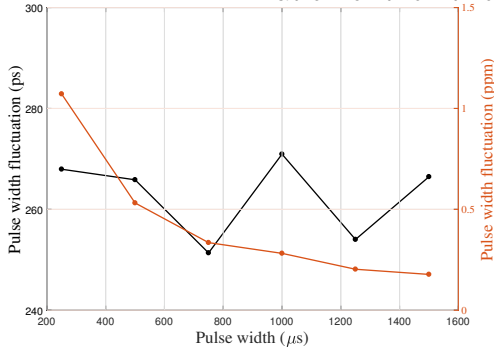


Figure 9: Pulse width distribution (500 pulses, 10 V height) as a function of the pulse width shown in absolute (black curve and left vertical axis) and relative (orange curve and right vertical axis) scale. For signals wider than  $\sim 500 \mu\text{s}$ , the fluctuations stays below 0.5 ppm.

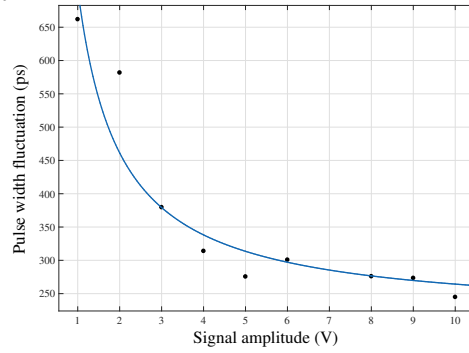


Figure 10: Pulse width distribution (500 pulses, 250  $\mu\text{s}$  wide) as a function of the pulse amplitude. At larger amplitude value, the relative magnitude of the oscilloscope front-end noise decreases allowing to reaching enhanced sensitivities.

from the pulser board, has a minimum for  $\sigma_{T_O}^2 = \sigma_{T_T}^2 + 8\tau^2\gamma^2 \sim 280 \text{ ps}$ , dominated by the voltage resolution of the RTO1044 oscilloscope. In such condition,  $\sigma_{T_O}$  has to be considered as an upper limit of the intrinsic calibrating pulse fluctuation.

Figure 8 shows the typical pulse width distribution acquired with the RTO1044

oscilloscope generating a sequence of 500 pulses, 10 V height, 250 ps wide. The measure was performed keeping the pulser board in a VOTSCH VT-7004 climatic chamber, at a stable temperature of 20°C. The distribution is well described by a Gaussian function centered at the average measured pulse width, whose standard deviation  $\sigma_{T_O} \sim 270$  ps describes the observed width fluctuation. Since the normal distribution fits the data, then the pulse width fluctuation is only due to random effects. In particular, neither clock transition miscounting nor missed triggers was observed. This proves the goodness of the design hardware choice and the satisfactory operation of the firmware. This procedure has been repeated at various pulse widths and amplitudes. The pulse width fluctuation as a function of  $T$  and  $V_0$  is shown in Fig.9 and Fig.10.  $\sigma_{T_O}$  remains constant with respect to the pulse width and it is close to the setup sensitivity, limited to  $\sim 280$  ps by the resolution of the digital conversion. This proves the pulser contribution is much lower than the measurement sensitivity. The observed pulse width fluctuation as a function of the signal amplitude, shown in Fig.10, decreases inversely proportional to the pulse amplitude until reaching the best available sensitivity for signals larger than 4 V. The larger time fluctuation at lower amplitude is due to noisy effects that are independent of the signal amplitude, such as the electric noise of the oscilloscope front-end or that of the pulser output buffer stage. Nevertheless, the contribution of the oscilloscope at low amplitudes is expected to be several times larger than that of the pulser board. Considering a typical calibrating pulse of  $T = 500 \mu s$ , the expected contribution to the intrinsic calibrating energy resolution is:

$$\left(\frac{dE}{E}\right)_T \leq \frac{\sigma_{T_O}}{T} \sim 1 \text{ ppm} \quad (24)$$

## 6 Baseline stabilization

The design of the pulse generation board makes the device able to deliver at its outputs not only calibrating pulse but also a constant voltage level and, eventually, to superimpose pulses over it. The capability of providing an adjustable and precise static level is very useful to optimize the operating temperature of the detector and to stabilize its baseline with respect to the low frequency drift due to the cryogenic setup. In particular, a settable power can be injected towards the detector by means of heaters located at the mixing chamber. The consequent temperature increase can be measured by cryogenic thermometers read out by the on-board 24-bit, dual differential channel, AD7732 Analog-to-Digital converter, from Analog Devices. This signal is compared to the target temperature and the power is adjusted to minimize the mismatch. Such closed-loop architecture must be customized to take into account the open-loop response of the cryostat. In particular, a proportional-integral-derivative (PID) controller can be implemented in software to manage the feedback mechanism. The pulse generation board, being able to provide power and read out the temperature, represents the core of the PID system, either if its calculation capability is exploited to implement the PID in the device firmware or if it is controlled by a remote master.

This baseline stabilization technique is currently used in the CUORE and CUPID-0 experiment. Figure 11 shows the effectiveness of this approach to compensate the low frequency baseline drift in one of the CUORE crystals. The orange curve shows the unavoidable large instabilities which usually occur in the detector baseline in a 9 hour run. As the baseline drift are proportional to the crystal temperature variation,

they must be continuously monitored and correlated to the detector response to ensure stability and reproducibility over the experiment lifetime. Superimposed to the orange curve, the blue line represents the baseline of the same detector in a 9 hour run in which the PID controller based on the pulse generation board is used. As it can be easily seen, the detector baseline stability is greatly improved and the intrinsic instabilities of the cryogenic system are completely compensated.

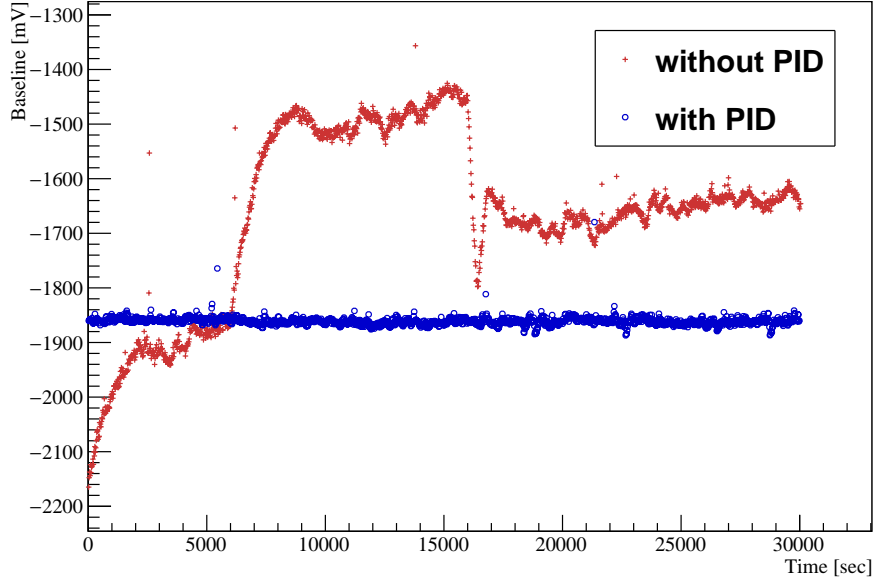


Figure 11: Bolometer baseline acquired in the CUORE experiment with the PID controller activated (blu line) or deactivated (orange line).

Beside the baseline stability, the PID controller can be also used to optimize the operating temperature of the crystals. Although the particle signals become larger at lower temperatures, as the thermal capacitance of the crystals decreases, the resistance of the NTD thermistors steeply increases up to  $1\text{ G}\Omega$  or more. Such condition are not compatible with a remote readout electronics at ambient temperature as the signals would be filtered on the large capacitance of the long connections driven by such a large resistors. Moreover, the whole system would be more sensitive to cross-talk, vibrational frictions and parallel noise of the input voltage sensitive amplifier. As the result, the operating temperature must be optimized to balance the contributions of NTDs and crystals and accomplish the best signal-to-noise performance. As the range of the power injected at the mixing chamber can be easily adjusted by set the attenuating factor of the output block (see Eq.3), target temperature of the PID controller can be set over a wide range. This ensures a high baseline stability at a temperature that fits the overall experimental needs.

## 7 Conclusions

In this paper, a circuit able to provide ultra-stable and ultra-precise pulses has been presented. The device has been specifically designed provide reference thermal signals via Joule effect useful to calibrate bolometric detectors. The pulse generation board is currently used in several experiments (CUORE, LUCIFER, CUPID-0, COSINUS, at LNGS) where it proved to be capable to stabilize the bolometer response against the instabilities usually affecting such cryogenic measurements. The pulse delivery and all the other features can be fully controlled and monitored from remote through a optically decoupled CAN bus. An additional daisy-chained optical trigger is also available. The designed choices has been presented in details. After undergoing a calibration procedures, a pulse energy stability of the order of 0.1 ppm/°C has been achieved in the temperature range of interest (20°C - 60°C). Moreover, an energy resolution of  $\sim 10$  eV FWHM has been accomplished for typical 1 MeV calibrating pulse thanks to the low electrical noise and the high timing precision. The pulser board can be also used in close-loop architecture (such as PID controllers) to compensate for the slow instabilities of the detector baseline and to optimize its operating temperature to achieve the best signal-to-noise ratio.

## References

- [1] A. Alessandrello et al., *Methods for response stabilization in bolometers for rare decays*, *Nucl. Instrum. Methods Phys. Res., Sect. A* **412-2** (1998) 454-464.
- [2] C. Arnaboldi et al., *Results from a search for the  $0\nu\beta\beta$ -decay of  $^{130}\text{Te}$* , *Phys. Rev., Sect. C* **78-035502** (2008).
- [3] C. Arnaboldi et al., *A programmable calibrating pulse generator with multi-outputs and very high stability*, *IEEE Transactions on Nuclear Science* **50** (2003) 979-986.
- [4] C. Arnaboldi et al., *A very high performance stabilization system for large mass bolometer experiments*, *Nucl. Instrum. Methods Phys. Res., Sect. A* **652** (2011) 306-309.
- [5] C. Arnaboldi et al., *CUORE: a cryogenic underground observatory for rare events*, *Nucl. Instrum. Methods Phys. Res., Sect. A* **518-3** (2004) 775-798.
- [6] D. R. Artusa et al., *Exploring the neutrinoless double beta decay in the inverted neutrino hierarchy with bolometric detectors*, *Eur. Phys. J. C* **74** (2014) 3096.
- [7] J. W. Beeman et al., *Current status and future perspectives of the LUCIFER experiment*, *Adv. High Energy Phys.* **237973** (2013).
- [8] D. R. Artusa et al., *Enriched  $\text{TeO}_2$  bolometers with active particle discrimination: towards the CUPID experiment*, *Phys. Lett. B* **767** (2017) 321-329.
- [9] G. Angloher et al., *The COSINUS project: perspectives of a NaI scintillating calorimeter for dark matter search*, *Eur. Phys. J. C* **76** (2016) 441.